IOP Publishing Journal of Physics: Condensed Matter
J. Phys.: Condens. Matter **33** (2021) 434001 (8pp) https://doi.org/10.1088/1361-648X/ac16f8

Complexities at the Au/ZrS_3(001) interface probed by x-ray photoemission spectroscopy

Archit Dhingra[1], Alexey Lipatov[2], Alexander Sinitskii[2] and Peter A Dowben[1,*]

[1] Department of Physics and Astronomy, University of Nebraska–Lincoln, Jorgenson Hall, 855 North 16th Street, Lincoln, NE 68588-0299, United States of America
[2] Department of Chemistry, University of Nebraska–Lincoln, Hamilton Hall, 639 North 12th Street, Lincoln, NE 68588-0304, United States of America

E-mail: pdowben1@unl.edu

Received 29 May 2021, revised 14 July 2021
Accepted for publication 22 July 2021
Published 12 August 2021

Abstract
Interaction between the Au adlayers and ZrS_3(001) has been examined via x-ray photoemission spectroscopy (XPS). The angle-resolved XPS measurements reveal that ZrS_3(001) is disulfide (S_2^{2-}) terminated and the Au thickness-dependent XPS indicates that the observed band bending, for low Au coverage, is consistent with formation of a Schottky barrier at the Au/ZrS_3(001) interface. This band bending, however, appears to be suppressed as the thickness of Au adlayer is increased, indicating varying interfacial interactions at the Au/ZrS_3(001) interface. Such complex interface effects between Au and ZrS_3(001) may explain the observed non-ohmic I–V characteristics for a ZrS_3-based device, and could suppress current injection.

Keywords: Schottky-barrier formation, 2D materials, quasi-1D trichalcogenides

(Some figures may appear in colour only in the online journal)

Transition metal trichalcogenides (TMTs), bearing the form MX_3 (M = Ti, Ta, Zr, Hf; X = S, Se, Te), are two-dimensional (2D) van der Waals materials that have garnered great interest owing to their versatility, as these materials find enormous applications in electronics [1–8], thermoelectrics [9–12], energy storage [13–16], photocatalysis [17, 18], and optoelectronics [2, 19–30]. As a consequence of their precise quasi-one-dimensional (quasi-1D) structure, TMT crystals lack edge disorders and dangling bonds [31], which project them as promising candidates for fabrication of transistors with widths of 10 nm or less. Thus, semiconducting TMTs are superior to other well-studied 2D materials as it is now known that graphene, graphene-based materials, and transition metal dichalcogenides are scourged with such unwanted edge effects. Nonetheless, there is an apparent disparity between the predicted (~1800–2500 $cm^2\ V^{-1}\ s^{-1}$) [32, 33] and measured (~10–30 $cm^2\ V^{-1}\ s^{-1}$ [34, 35] or less [36]) charge carrier mobilities for ZrS_3, which should be addressed if device applications are to be realized.

In light of this disagreement between theory [32, 33] and experiment [34, 35] regarding the expected and measured mobilities of ZrS_3, both phonon scattering and contact problems must be considered. A recent study [36], which focused on understanding the possible detrimental effects of phonon vibrations on carrier mobility of ZrS_3, revealed that the electron–phonon scattering in this material may not be completely responsible for low observed mobilities, as the ZrS_3 lattice is quite stiff. Indeed, ZrS_3 is found to be stiffer than TiS_3, where phonon scattering does play a significant role in suppressing mobility [6]. Nevertheless, this disparity between the expected and measured mobilities of ZrS_3 could be a consequence of the formation of either a Schottky barrier at the

* Author to whom any correspondence should be addressed.

 © 2021 IOP Publishing Ltd Printed in the UK

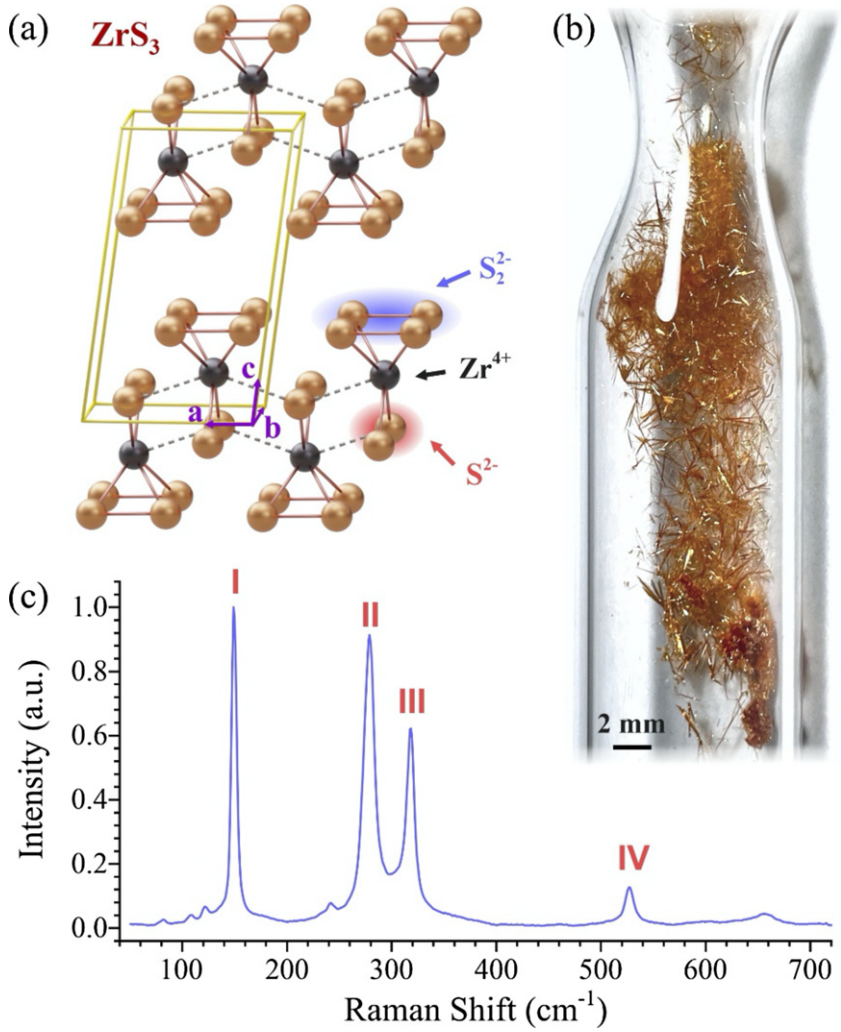

Figure 1. (a) The crystal structure of ZrS_3. (b) A vacuum-sealed quartz ampule with ZrS_3 crystals. (c) The Raman spectrum of ZrS_3 crystals.

metal–semiconductor interface (since a high work function metal, like Au [37, 38], is expected to form a Schottky barrier when brought in contact with an n-type semiconductor with a relatively low work function [39]) or a very complicated Au/ZrS_3 interface that limits efficient charge injection. Deciphering this is crucial since both, presence of a Schottky barrier (or absence of a good ohmic contact) [40, 41] and less efficient charge injection [42–44], are known to degrade the measured transistor mobilities in a device. Therefore, in this work, we have employed x-ray photoemission spectroscopy (XPS) to study the interface between Au adlayers of varied thickness and the n-type ZrS_3(001) [10, 45–47] to understand whether reproducing interfaces, with low contact potential, is even likely.

Figure 1(a) shows the crystal structure of ZrS_3, which belongs to the $P2_1/m$ space group with the lattice constants being $a = 5.1107(4)$ Å, $b = 3.6179(2)$ Å, $c = 8.9725(5)$ Å, and the cant angle $\beta = 97.64(1)°$, as reported in the literature elsewhere [45]. The ZrS_3 structure contains 2D layers that are parallel to the *ab* plane of the unit cell (figure 1(a)). The 2D layers, in turn, are composed of quasi-1D chains of trigonal prisms formed by sulfide (S^{2-}) and disulfide (S_2^{2-}) units with Zr^{4+} in the center; the quasi-1D chains are oriented along the *b* direction (figure 1(a)). The ZrS_3 crystals were synthesized through a reaction between metallic zirconium and sulfur vapor in vacuum-sealed quartz ampules at 800 °C, as has been described previously [48, 49]. After two weeks of annealing at 800 °C, numerous 1–2 mm long ZrS_3 crystals were formed, as shown in figure 1(b). These crystals were characterized by Raman spectroscopy using a Thermo Scientific DXR Raman microscope with a 532 nm excitation laser. The Raman spectrum in figure 1(c) shows four major peaks at 149 cm^{-1} (I), 279 cm^{-1} (II), 318 cm^{-1} (III) and 527 cm^{-1} (IV), which are characteristic for ZrS_3 [28, 43, 44].

All the core-level XPS measurements were performed in an ultra-high vacuum (UHV) chamber with a base pressure better than 8×10^{-10} mbar, using a SPECS x-ray Al anode ($h\nu = 1486.6$ eV) as the source and a hemispherical electron analyzer (PHI model: 10–360) that has an angular acceptance of ±10°. The ZrS_3 crystals were exfoliated inside the UHV chamber to produce a freshly cleaved surface for the XPS analysis. The resulting surface of ZrS_3 that was studied here is the (001) surface, since ZrS_3 is isostructural with TiS_3 [20, 36, 45], and for TiS_3 the most likely cleavage plane is (001) (as was

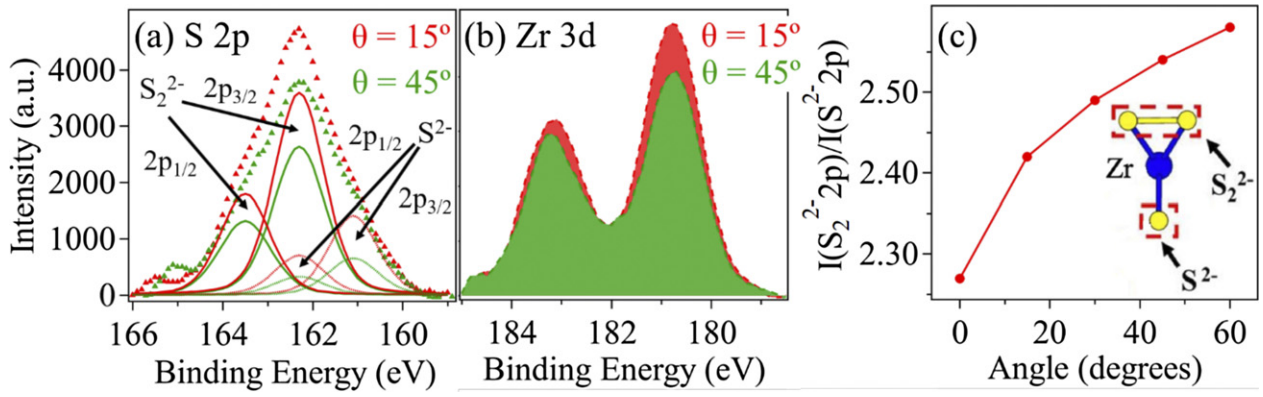

Figure 2. ARXPS measurements of ZrS_3(001). (a) The raw photoemission spectrum of the S 2p core-level collected at 15° (red) and 45° (green) along with the fits showing S^{2-} $2p_{3/2}$ (161.1 eV), S^{2-} $2p_{1/2}$ (162.3 eV), S_2^{2-} $2p_{3/2}$ (162.3 eV), and S_2^{2-} $2p_{1/2}$ (163.5 eV) core-level components. (b) The raw photoemission spectra of the Zr 3d core-level obtained at 15° (red) and 45° (green). (c) XPS peak intensity ratios of the S_2^{2-} $2p_{3/2}$ and S^{2-} $2p_{3/2}$ core-level components as a function of take-off angle with respect to the surface normal. The inset shows a schematic of a fragment of the ZrS_3 structure, highlighting the two different types of sulfur species (S^{2-} and S_2^{2-}).

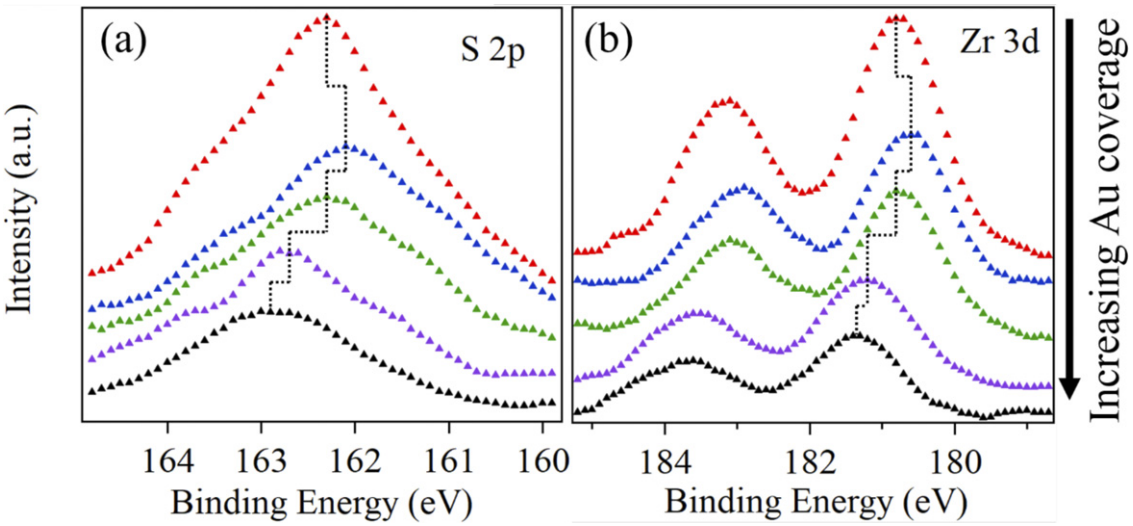

Figure 3. The XPS spectra of the (a) S 2p and (b) the Zr 3d core-level components of Au/ZrS_3(001) with increasing thickness of Au adlayer. The vertical dashed lines denote the peak XPS binding energies of S 2p and Zr 3d core-levels, whereas the horizontal dashed lines denote the shifts in binding energies. The red spectra (at top) correspond to 0 Å of Au (i.e. the bare ZrS_3(001)), the blue spectra correspond to 4 Å of Au, the green spectra correspond to 8 Å of Au, the purple spectra correspond to 12 Å of Au, and the black spectra correspond to 16 Å of Au, respectively.

shown both theoretically and experimentally [31]). This is also consistent with the experimental band structures obtained for ZrS_3(001) as reported elsewhere [20, 45] following a similar procedure.

The angle-resolved x-ray photoemission spectroscopy (ARXPS) data were collected by changing the photoemission take-off angle between 0–60°, with respect to the surface normal. The Au adlayers were physically evaporated onto the ZrS_3(001) crystals by resistively heating Au wires in a tungsten basket, as described elsewhere [3]. A thickness monitor was used to ascertain the thickness of the deposited Au adlayers, as was done in our previous work [50].

The XPS spectra of the S 2p and Zr 3d core-levels of ZrS_3 collected at 15° (red) and 45° (green) are shown in figures 2(a) and (b), respectively. It is observed that the S 2p core-level of this material has four distinct features (figure 2(a)), namely: S^{2-} $2p_{3/2}$ (161.1 eV), S^{2-} $2p_{1/2}$ (162.3 eV), S_2^{2-} $2p_{3/2}$ (162.3 eV), and S_2^{2-} $2p_{1/2}$ (163.5 eV), which are consistent with the existing literature [36]. From figure 2(b), the Zr $3d_{5/2}$ and Zr $3d_{3/2}$ core-level components of this system are identified at the binding energies of 180.8 eV and 183.2 eV, respectively, which are in close agreement with the reported binding energies for these core-levels [51, 52]. Furthermore, the angle-dependent photoemission peak intensity ratios of the disulfide (S_2^{2-}) $2p_{3/2}$ core-level and sulfide (S^{2-}) $2p_{3/2}$ core-level components (shown in figure 2(c)) indicate that ZrS_3(001) terminates in S_2^{2-} (highlighted in figure 1(a) and the inset in figure 2(c)), which agrees with our expectations since ZrS_3 possesses the same structure as TiS_3 [20, 36, 45].

The photoemission spectra of the S 2p and Zr 3d core-levels of Au/ZrS_3(001) with varying Au adlayer thickness are shown

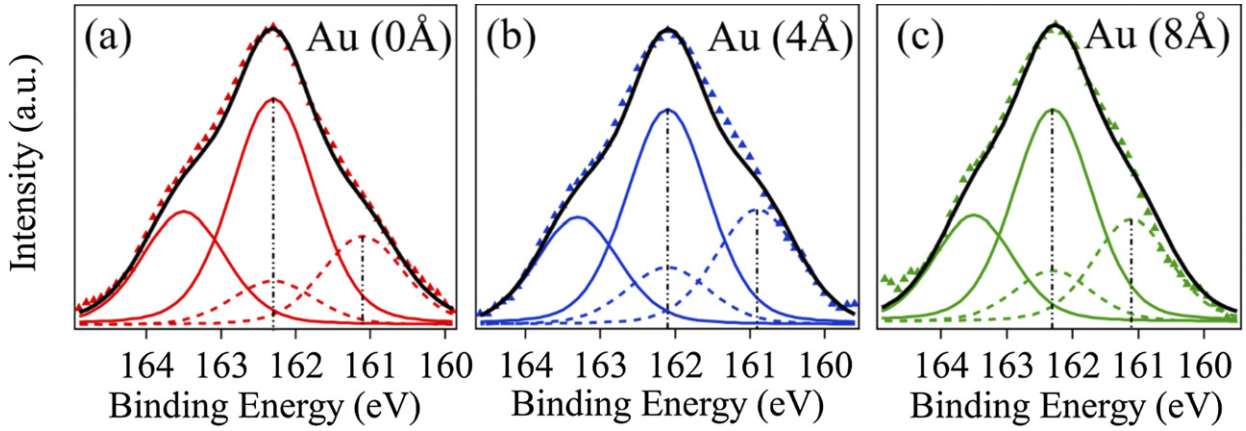

Figure 4. Photoemission spectra of the S 2p core-level of Au/ZrS_3(001) with (a) 0 Å of Au (bare ZrS_3(001)), (b) 4 Å of Au, and (c) 8 Å of Au, respectively. The dashed lines at 161.1 eV and 162.3 eV in both (a) and (c) mark the binding energies of the S^{2-} $2p_{3/2}$ and S_2^{2-} $2p_{3/2}$ core-level components, respectively. Whereas the binding energies of the S^{2-} $2p_{3/2}$ and S_2^{2-} $2p_{3/2}$ core-level components in (b) are indicated by the dashed lines at 160.9 eV and 162.1 eV, respectively. The solid black lines show the fit results.

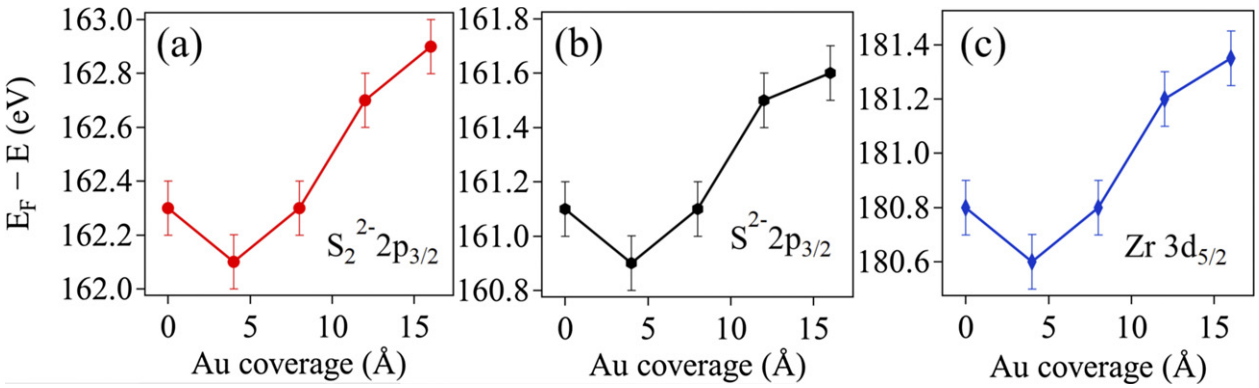

Figure 5. Change in the peak XPS binding energies of the (a) S_2^{2-} $2p_{3/2}$, (b) S^{2-} $2p_{3/2}$ and (c) Zr $3d_{5/2}$ core-level features of Au/ZrS_3(001) with varying Au coverage. The solid lines connecting the data points are a guide for the eye. Here, error bars represent what are largely the systematic errors.

in figures 3(a) and (b), respectively. From these figures, it can be seen that the peak XPS binding energies for both the core-levels are shifted toward a lower value as the thickness of Au adlayer is increased from 0 Å (spectra shown in red in figure 3) to 4 Å (spectra shown in blue in figure 3). However, it is also observed that further increment of the Au adlayer thickness shifts the peak XPS binding energies of the S 2p and Zr 3d core-levels toward higher values. Explanation for such a trend in the binding energy shifts with different thicknesses of Au adlayer, which may seem confusing at first glance, is presented in detail below.

Figure 4(a) shows the XPS spectrum of the S 2p core-level of bare ZrS_3(001) along with the fits showing the S^{2-} $2p_{3/2}$ and S_2^{2-} $2p_{3/2}$ core-level components at the binding energy values of 161.1 eV and 162.3 eV, respectively. With an increase in Au thickness from 0 Å to 4 Å (figure 4(b)), there is a shift in the binding energies of the S^{2-} $2p_{3/2}$ and S_2^{2-} $2p_{3/2}$ core-level components. The binding energy of the S^{2-} $2p_{3/2}$ core-level is found to be shifted to a lower value of 160.9 eV and the binding energy of the S_2^{2-} $2p_{3/2}$ core-level is now shifted to 162.1 eV. This shift (of ∼0.2 eV) to lower binding energy values implies an upward band bending, which may be indicative of a Schottky-barrier formation [39] at the Au/ZrS_3(001) interface. For an n-type semiconductor, the band bending is upward for the formation of a Schottky barrier at the metal–semiconductor interface [39]. Absent interface interactions, Schottky barrier formation is expected because ZrS_3 is n-type semiconductor [10, 20, 34, 40, 44], and Au has a large work function (5.1 eV [38] to 5.4 eV [37, 38]), much greater than the work function of ZrS_3. From the cutoff of the secondary electrons, we have determined that the work function of ZrS_3 lies between 3.8 and 4.4 eV.

That said, strong interactions at the Au–ZrS_3 interface are indicated. With a further increase in the Au adlayer thickness from 4 Å to 8 Å (figure 4(c)) there is a complete suppression of Schottky barrier-like band bending, as is illustrated by a shift in the binding energy values of the S^{2-} $2p_{3/2}$ and S_2^{2-} $2p_{3/2}$ core-levels back to what they were for the bare ZrS_3(001), as very clearly illustrated in figure 5. This observed suppression of a possible Schottky barrier at the Au/ZrS_3(001) interface, which occurs as the thickness of Au adlayer is increased more than 4 Å, is most likely a consequence of Au–S

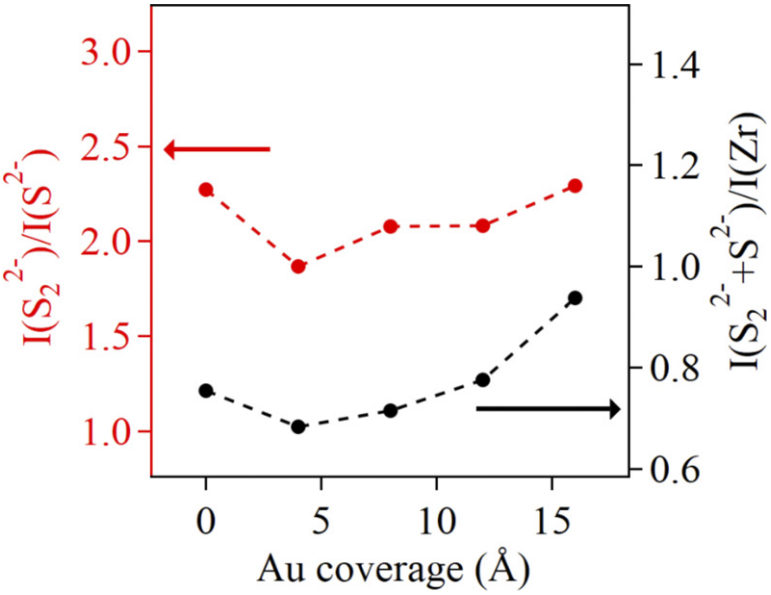

Figure 6. XPS peak intensity ratios of the S_2^{2-} $2p_{3/2}$ and S^{2-} $2p_{3/2}$ core-level components as a function of Au coverage are shown in red, whereas the XPS peak intensity ratios of the $2p_{3/2}$ core-level components of the two sulfurs combined ($S_2^{2-} + S^{2-}$) to the $3d_{5/2}$ core-level of Zr as a function of Au coverage are shown in black. For reference, for three S atoms and one Zr atom, ratio of the combined $2p_{3/2}$ core-levels of ($S_2^{2-} + S^{2-}$) to the Zr $3d_{5/2}$ core-level would correspond to ∼0.96.

[53, 54] and Au–Zr [55–59] interactions. This is because an increase in binding energies of the S 2p and Zr 3d core-levels implies that the Au–S and Au–Zr chemical interactions are responsible for the downward bending of the bands (away from the Fermi level (E_F)), which actually opposes the upward band bending that occurs due to the formation of a Schottky barrier. Our results are consistent with the observed Schottky barrier suppression in n-type TiS_3 [6, 60] as a result of strong Au–S interactions [3].

The changes in binding energies of the S_2^{2-} $2p_{3/2}$, S^{2-} $2p_{3/2}$ and Zr $3d_{5/2}$ core-level features of Au/ZrS_3(001) with increase in Au coverage are shown in figures 5(a)–(c), respectively. Since the dependence of binding energies on Au coverage for all these core-level components follow more or less the same trend, it can be inferred that with increasing Au coverage any tendency towards the formation of Schottky barrier at the Au/ZrS_3(001) interface is overwhelmed by strong Au–S and Au–Zr interactions, as noted above, that are enhanced as the thickness of the Au adlayer is increased. And the strengthening of these Au adlayer thickness dependent interactions is reflected in the elevated core-level binding energies as the Au coverage is increased above 4 Å. Additionally, a closer examination of figure 5 reveals that the shift in the binding energy of the S_2^{2-} $2p_{3/2}$ core-level of Au/ZrS_3(001) for 16 Å of Au is +0.6 eV in reference to the S_2^{2-} $2p_{3/2}$ core-level binding energy in absence of Au, whereas the shifts in the binding energies of the S^{2-} $2p_{3/2}$ and Zr $3d_{5/2}$ core-levels under the same conditions are +0.5 eV and +0.55 eV, respectively. In other words, figure 5 implies that the interaction of S_2^{2-} with Au is stronger than that of Zr with Au (which is still stronger than the interaction of S^{2-} with Au), which is in line with our surface termination results (shown in figure 2(c)).

Additionally, the trend seen for the dependence of binding energies of the core-levels on Au coverage (figure 5) is also reflected in the dependence of XPS peak intensity ratios on Au coverage, which are shown in figure 6. The S_2^{2-} $2p_{3/2}$ core-level relative to the S^{2-} $2p_{3/2}$ core-level peak intensity ratio is not precisely ∼2:1 (see the red curve in figure 6) because of the dominant S_2^{2-} disulfide surface termination of ZrS_3(001) which in turn makes the S_2^{2-} $2p_{3/2}$ core-level relatively stronger and, overall, since XPS is a highly surface sensitive characterization technique. The sudden dip in the XPS peak intensity of the S_2^{2-} $2p_{3/2}$ core-level relative to the S^{2-} $2p_{3/2}$ core-level seen for 4 Å of Au adlayer thickness (see the red curve in figure 6) is consistent with the fact that ZrS_3(001) terminates in S_2^{2-} and, hence, more of the S_2^{2-} interacts with Au than S^{2-} does. For further increments in the Au adlayer thickness, the S_2^{2-} $2p_{3/2}$ core-level relative to the S^{2-} $2p_{3/2}$ core-level peak intensity tends to increase due to the Au–S formation (which occurs as a result of interaction of S^{2-} with Au), and also suggests sulfur replacement at the Au/ZrS_3(001) interface. Thus, thicker depositions of Au adlayers will lead to a decrease in the peak XPS intensity of the S^{2-} 2p core-level, although the ratio of disulfide to sulfide (S_2^{2-}:S^{2-}) remains roughly 2 (see the red curve in figure 6).

The black curve in figure 6 illustrates that the XPS peak intensity ratios of the combined sulfur ($S_2^{2-} + S^{2-}$) $2p_{3/2}$ core-levels to the $3d_{5/2}$ core-level of Zr decrease with increasing Au thickness. This ratio primarily depends on the XPS intensity of the S_2^{2-} $2p_{3/2}$ core-level not only due to the disulfide surface termination of ZrS_3(001) but also because of the possibility of gold sulfide formation. Therefore, the XPS peak intensity ratio I($S_2^{2-} + S^{2-}$)/I(Zr) increases as the Au adlayer

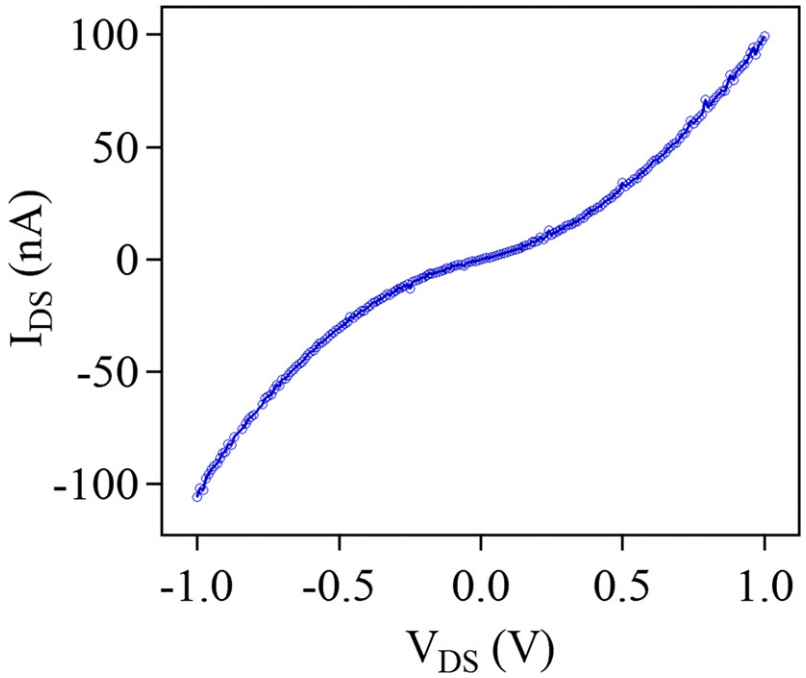

Figure 7. The I–V curve obtained from a ZrS_3 FET with Au electrodes at zero gate bias. The ZrS_3 semiconductor channel is roughly 70 nm high and 1 μm wide.

thickness is increased beyond 4 Å. The nature of this increment in the I(S_2^{2-} + S^{2-})/I(Zr) ratio is such that the eventually, at an Au coverage of 16 Å or more, the I(S_2^{2-} + S^{2-})/I(Zr) ratio is larger than what was observed for bare ZrS_3(001).

Furthermore, unlike the case of Au/TiS_3 interface [3], where the field effect transistor (FET) measurements confirm that the Au contacts are essentially ohmic, we see that the I–V curve for our ZrS_3 device (shown in figure 7) is non-ohmic. As noted above, the non-ohmic nature of this I–V curve can be understood as the effect of barriers to charge injection at the Au/ZrS_3 interface, which, for small bias voltages, is a consequence of the strong, but complex, Au–S and Au–Zr interactions. It is the strong Au to sulfur interaction that appears to overcome the tendency for Au to form a Schottky barrier with TiS_3 [3], which would be expected as a result of the large work function of Au. It is expected that the Zr to S interaction are stronger than Ti to S given that the Ti–S bond energy is about 4.4 eV while the Zr–S bond is about 6 eV. Given the likely strong sulfur to zirconium bond strength, the S interactions with Au at the ZrS_3 interface may not be sufficient for formation of an ohmic like contact. The interface between Au and ZrS_3(001) is, nonetheless, driven by Au–S interactions, suggesting that gold sulfide compound formation may occur at the interface, as is also suggested by the Au core level spetrum (supplementary materials).

The device measurements are consistent with the XPS data. Our ARXPS results indicate that the Au–S_2^{2-} interaction is more significant than the Au–S^{2-} and Au–Zr interactions. As reported elsewhere [36], the measured transistor mobilities for TiS_3 are 10^5 greater than ZrS_3, consistent with the fact that the Au–TiS_3 interface is largely ohmic [3, 6], which is not seen here for ZrS_3.

In conclusion, our Au thickness-dependent XPS measurements indicate the presence of band bending at the Au/ZrS_3(001) interface for very low thickness (∼4 Å) of Au adlayer. However, this Schottky-barrier type band bending is easily suppressed owing to the strong Au–S and Au–Zr interactions that become increasingly evident as the Au coverage is increased further. The interface interactions between Au and ZrS_3(001) are consistent with our ARXPS results as the Au–S_2^{2-} interaction is found to be more significant than Au–S^{2-} and Au–Zr. It is expected that the Zr to S interaction is stronger than Ti to S, thus the S interactions with Au at the ZrS_3 interface may not be sufficient for formation of an ohmic like contact seen with TiS_3 [3]. The interactions at the Au/ZrS_3(001) interface may be one of the major factors that adversely affect the performance of ZrS_3-based devices with Au contacts with thicknesses >15 nm. This is consistent with (and also explains) the observed non-ohmic behavior of the I–V curve for a ZrS_3 device [20].

Acknowledgments

This research was supported by the National Science Foundation (NSF), through Grant No. NSF-ECCS 1740136, as well as by the nCORE, which is a wholly owned subsidiary of the Semiconductor Research Corporation (SRC), through the Center on Antiferromagnetic Magneto-electric Memory and Logic Task No. 2760.002.

Data availability statement

All data that support the findings of this study are included within the article and supplementary files.

ORCID iDs

Archit Dhingra https://orcid.org/0000-0001-9352-4361
Alexey Lipatov https://orcid.org/0000-0001-5043-1616
Alexander Sinitskii https://orcid.org/0000-0002-8688-3451
Peter A Dowben https://orcid.org/0000-0002-2198-4710

References

[1] Island J O *et al* 2015 TiS_3 transistors with tailored morphology and electrical properties *Adv. Mater.* **27** 2595–601
[2] Island J O *et al* 2016 Titanium trisulfide (TiS_3): a 2D semiconductor with quasi-1D optical and electronic properties *Sci. Rep.* **6** 1–7
[3] Gilbert S J, Lipatov A, Yost A J, Loes M J, Sinitskii A and Dowben P A 2019 The electronic properties of Au and Pt metal contacts on quasi-one-dimensional layered TiS_3(001) *Appl. Phys. Lett.* **114** 101604
[4] Lipatov A, Wilson P M, Shekhirev M, Teeter J D, Netusil R and Sinitskii A 2015 Few-layered titanium trisulfide (TiS_3) field-effect transistors *Nanoscale* **7** 12291–6
[5] Molina-Mendoza A J *et al* 2017 High current density electrical breakdown of TiS_3 nanoribbon-based field-effect transistors *Adv. Funct. Mater.* **27** 1605647
[6] Randle M *et al* 2018 Gate-controlled metal–insulator transition in TiS_3 nanowire field-effect transistors *ACS Nano* **13** 803–11
[7] Xiong W-W, Chen J-Q, Wu X-C and Zhu J-J 2014 Individual HfS_3 nanobelt for field-effect transistor and high performance visible-light detector *J. Mater. Chem.* C **2** 7392
[8] Dai J and Zeng X C 2015 Titanium trisulfide monolayer: theoretical prediction of a new direct-gap semiconductor with high and anisotropic carrier mobility *Angew. Chem., Int. Ed.* **54** 7572–6
[9] Zhang J, Liu X, Wen Y, Shi L, Chen R, Liu H and Shan B 2017 Titanium trisulfide monolayer as a potential thermoelectric material: a first-principles-based Boltzmann transport study *ACS Appl. Mater. Interfaces* **9** 2509–15
[10] Morozova N V, Korobeinikov I V, Kurochka K V, Titov A N and Ovsyannikov S V 2018 Thermoelectric properties of compressed titanium and zirconium trichalcogenides *J. Phys. Chem.* C **122** 14362–72
[11] Sakuma T, Nishino S, Miyata M and Koyano M 2018 Thermoelectric properties for a suspended microribbon of quasi-one-dimensional TiS_3 *J. Electron. Mater.* **47** 3177–83
[12] Guilmeau E, Berthebaud D, Misse P R N, Hébert S, Lebedev O I, Chateigner D, Martin C and Maignan A 2014 $ZrSe_3$-Type variant of TiS_3: structure and thermoelectric properties *Chem. Mater.* **26** 5585–91
[13] Wu J, Wang D, Liu H, Lau W-M and Liu L-M 2015 An *ab initio* study of TiS_3: a promising electrode material for rechargeable Li and Na ion batteries *RSC Adv.* **5** 21455–63
[14] Tanibata N, Matsuyama T, Hayashi A and Tatsumisago M 2015 All-solid-state sodium batteries using amorphous TiS_3 electrode with high capacity *J. Power Sources* **275** 284–7
[15] Taniguchi K, Gu Y, Katsura Y, Yoshino T and Takagi H 2016 Rechargeable Mg battery cathode TiS_3 with d–p orbital hybridized electronic structures *Appl. Phys. Express* **9** 011801
[16] Arsentev M, Missyul A, Petrov A V and Hammouri M 2017 TiS_3 magnesium battery material: atomic-scale study of maximum capacity and structural behavior *J. Phys. Chem.* C **121** 15509–15
[17] Zhao Q, Guo Y, Zhou Y, Yao Z, Ren Z, Bai J and Xu X 2018 Band alignments and heterostructures of monolayer transition metal trichalcogenides MX_3 (M = Zr, Hf; X = S, Se) and dichalcogenides MX_2 (M = Tc, Re; X=S, Se) for solar applications *Nanoscale* **10** 3547–55
[18] Tian Z *et al* 2021 Efficient photocatalytic hydrogen peroxide generation coupled with selective benzylamine oxidation over defective ZrS_3 nanobelts *Nat. Commun.* **12** 2039
[19] Island J O *et al* 2014 Ultrahigh photoresponse of few-layer TiS_3 nanoribbon transistors *Adv. Opt. Mater.* **2** 641–5
[20] Gilbert S J *et al* 2020 Effect of band symmetry on photocurrent production in quasi-one-dimensional transition-metal trichalcogenides *ACS Appl. Mater. Interfaces* **12** 40525–31
[21] Hou S, Guo Z, Yang J, Liu Y Y, Shen W, Hu C, Liu S, Gu H and Wei Z 2021 Birefringence and dichroism in quasi-1D transition metal trichalcogenides: direct experimental investigation *Small* **17** 2100457
[22] Guo J *et al* 2020 Controllable thermal oxidation and photoluminescence enhancement in quasi-1D van der Waals ZrS_3 flakes *ACS Appl. Electron. Mater.* **2** 3756–64
[23] Cui Q, Lipatov A, Wilt J S, Bellus M Z, Zeng X C, Wu J, Sinitskii A and Zhao H 2016 Time-resolved measurements of photocarrier dynamics in TiS_3 nanoribbons *ACS Appl. Mater. Interfaces* **8** 18334–8
[24] Ferrer I J, Ares J R, Clamagirand J M, Barawi M and Sánchez C 2013 Optical properties of titanium trisulphide (TiS_3) thin films *Thin Solid Films* **535** 398–401
[25] Niu Y *et al* 2018 Polarization-sensitive and broadband photodetection based on a mixed-dimensionality TiS_3/Si p-n junction *Adv. Opt. Mater.* **6** 1800351
[26] Talib M, Tabassum R, Abid I S S, Islam S S and Mishra P 2019 Improvements in the performance of a visible-NIR photodetector using horizontally aligned TiS_3 nanoribbons *ACS Omega* **4** 6180–91
[27] Liu S, Xiao W, Zhong M, Pan L, Wang X, Deng H-X, Liu J, Li J and Wei Z 2018 Highly polarization sensitive photodetectors based on quasi-1D titanium trisulfide (TiS_3) *Nanotechnology* **29** 184002
[28] Wang X *et al* 2019 Highly polarized photoelectrical response in vdW ZrS_3 nanoribbons *Adv. Electron. Mater.* **5** 1900419
[29] Yang S *et al* 2019 Highly sensitive polarization photodetection using a pseudo-one-dimensional $Nb_{(1-x)}Ti_xS_3$ alloy *ACS Appl. Mater. Interfaces* **11** 3342–50
[30] Tao Y-R, Wu J-J and Wu X-C 2015 Enhanced ultraviolet-visible light responses of phototransistors based on single and a few ZrS_3 nanobelts *Nanoscale* **7** 14292–8
[31] Lipatov A *et al* 2018 Quasi-1D TiS_3 nanoribbons: mechanical exfoliation and thickness-dependent Raman spectroscopy *ACS Nano* **12** 12713–20
[32] Ahammed R, Rawat A, Jena N, Dimple, Mohanta M K and De Sarkar A 2020 ZrS_3/MS_2 and ZrS_3/MXY (M Mo, W; X, Y S, Se, Te; X $\neq$ Y) type-II van der Waals heterobilayers: prospective candidates in 2D excitonic solar cells *Appl. Surf. Sci.* **499** 143894
[33] Wang C, Zheng C and Gao G 2020 Bulk and monolayer ZrS_3 as promising anisotropic thermoelectric materials: a comparative study *J. Phys. Chem.* C **124** 6536–43
[34] Perluzzo G, Lakhani A A and Jandl S 1980 Electrical transport measurements in a quasi-onedimensional semiconductor ZrS_3 *Solid State Commun.* **35** 301–4
[35] Späh R, Lux-Steiner M, Bucher E and Wagner S 1984 n-ZrS_3/p-WSe_2 heterojunctions *Appl. Phys. Lett.* **45** 744–5
[36] Dhingra A, Lipatov A, Loes M J, Sinitskii A and Dowben P A 2021 Nonuniform Debye temperatures in

quasi-one-dimensional transition-metal trichalcogenides *ACS Mater. Lett.* **3** 414–9

[37] Potter H C and Blakely J M 1975 LEED, Auger spectroscopy, and contact potential studies of copper–gold alloy single crystal surfaces *J. Vac. Sci. Technol.* **12** 635–42

[38] Kawano H 2008 Effective work functions for ionic and electronic emissions from mono- and polycrystalline surfaces *Prog. Surf. Sci.* **83** 1–165

[39] Zhang Z and Yates J T 2012 Band bending in semiconductors: chemical and physical consequences at surfaces and interfaces *Chem. Rev.* **112** 5520–51

[40] Palmstrøm C J 2001 Contacts for compound semiconductors: ohmic type *Encyclopedia of Materials: Science and Technology* (Amsterdam: Elsevier) pp 1581–7

[41] Suemitsu T 2011 GaAs- and InP-based high-electron-mobility transistors *Comprehensive Semiconductor Science and Technology* (Amsterdam: Elsevier) pp 84–113

[42] Parto K, Pal A, Chavan T, Agashiwala K, Yeh C-H, Cao W and Banerjee K 2021 One-dimensional edge contacts to two-dimensional transition-metal dichalcogenides: uncovering the role of Schottky-barrier anisotropy in charge transport across MoS_2/metal interfaces *Phys. Rev. Appl.* **15** 064068

[43] Campbell I H, Kress J D, Martin R L, Smith D L, Barashkov N N and Ferraris J P 1997 Controlling charge injection in organic electronic devices using self-assembled monolayers *Appl. Phys. Lett.* **71** 3528

[44] Scott J C 2003 Metal-organic interface and charge injection in organic electronic devices *J. Vac. Sci. Technol.* A **21** 521

[45] Yi H, Gilbert S J, Lipatov A, Sinitskii A, Avila J, Abourahma J, Komesu T, Asensio M C and Dowben P A 2020 The electronic band structure of quasi-one-dimensional van der Waals semiconductors: the effective hole mass of ZrS_3 compared to TiS_3 *J. Phys.: Condens. Matter* **32** 29LT01

[46] Flores E, Ares J R, Ferrer I J and Sánchez C 2016 Synthesis and characterization of a family of layered trichalcogenides for assisted hydrogen photogeneration *Phys. Status Solidi RRL* **10** 802–6

[47] Gorochov O, Katty A, Le Nagard N, Levy-Clement C, Redon A and Tributsch H 1983 Photoelectrochemical behavior and light-induced anodic transformation of zirconium trisulfide *J. Electrochem. Soc.* **130** 1301–4

[48] Muratov D S, Vanyushin V O, Vorobeva N S, Jukova P, Lipatov A, Kolesnikov E A, Karpenkov D, Kuznetsov D V and Sinitskii A 2020 Synthesis and exfoliation of quasi-1D $(Zr,Ti)S_3$ solid solutions for device measurements *J. Alloys Compd.* **815** 152316

[49] Muratov D S *et al* 2019 Slot-die-printed two-dimensional ZrS_3 charge transport layer for perovskite light-emitting diodes *ACS Appl. Mater. Interfaces* **11** 48021–8

[50] Dhingra A *et al* 2020 Surface termination and Schottky-barrier formation of In_4Se_3(001) *Semicond. Sci. Technol.* **35** 065009

[51] Jellinek F, Pollak R A and Shafer M W 1974 X-ray photoelectron spectra and electronic structure of zirconium trisulfide and triselenide *Mater. Res. Bull.* **9** 845–56

[52] Zakharova O V, Gusev A A, Abourahma J, Vorobeva N S, Sokolov D V, Muratov D S, Kuznetsov D V and Sinitskii A 2020 Nanotoxicity of ZrS_3 probed in a bioluminescence test on *E. Coli* bacteria: the effect of evolving H_2S *Nanomaterials* **10** 1–10

[53] Biener M M, Biener J and Friend C M 2005 Revisiting the S–Au(111) interaction: static or dynamic? *Langmuir* **21** 1668–71

[54] Fan C-Y, Xiao P, Li H-H, Wang H-F, Zhang L-L, Sun H-Z, Wu X-L, Xie H-M and Zhang J-P 2015 Nanoscale polysulfides reactors achieved by chemical Au–S interaction: improving the performance of Li–S batteries on the electrode level *ACS Appl. Mater. Interfaces* **7** 27959–67

[55] Lomello-Tafin M, Galez P, Gachon J C, Feschotte P and Jorda J L 1997 The Zr–Au system *J. Alloys Compd.* **257** 215–23

[56] Okamoto H 1999 Au–Zr (gold–zirconium) *J. Phase Equil.* **20** 349–50

[57] Li Z-h, Jin Z-p and Liu H-s 2003 Thermodynamic assessment of Au–Zr system *J. Cent. S. Univ. Technol.* **10** 94–7

[58] Zhang K and Li J 2006 Partial phase diagram of the Au–Ag–Zr ternary system *J. Alloys Compd.* **417** 155–8

[59] Nozaki A *et al* 2016 Skeletal Au prepared from Au–Zr amorphous alloys with controlled atomic compositions and arrangement for active oxidation of benzyl alcohol *J. Mater. Chem.* A **4** 8458–65

[60] Yi H *et al* 2018 The band structure of the quasi-one-dimensional layered semiconductor TiS_3(001) *Appl. Phys. Lett.* **112** 052102